Nano Research

Open Access

Research Article

Speckle-free laser display enabled by self-assembled supraparticles of semiconductor nanoplatelets

Chenlin Wang[1], Haixiao Zhao[2], Xian Zhao[2,3], Baoqing Sun[1,2], and Yuan Gao[1,2]✉

[1] School of Information Science and Engineering, Shandong University, Qingdao 266237, China
[2] Key Laboratory of Laser & Infrared System (Shandong University), Ministry of Education, Shandong University, Qingdao 266237, China
[3] Center for Optics Research and Engineering (CORE), Shandong University, Qingdao 266237, China

Cite this article: *Nano Research*, **2025**, *18*, 94907170. https://doi.org/10.26599/NR.2025.94907170

ABSTRACT: Laser-based light sources are highly desirable for display applications due to their narrow emission linewidth and exceptional brightness. However, the coherence inherent in lasers often leads to the formation of unwanted speckles, which can significantly degrade display quality. Thus, there is a critical need for light sources that retain the narrow emission and high brightness of lasers while minimizing spatial coherence to reduce speckle formation. Random lasing has emerged as a promising strategy to address this issue, though its random emission directions can lead to energy losses. To overcome this challenge, we propose a novel approach in which CdSe nanoplatelets, known for their efficient optical gain properties, are self-assembled into supraparticles (SPs), serving as both scattering centers and gain media. This configuration enables random lasing, and by coupling the random gain medium to a Fabry–Pérot (FP) cavity, we successfully direct the typically omnidirectional random lasing into a controlled, low-coherence emission. Our experimental results, comparing conventional lasers (e.g., He:Ne lasers) with our SP-based laser for a projector, demonstrate effective suppression of speckle formation, reducing speckle contrast from 0.5 to 0.05. These findings offer a promising solution for improving the performance and quality of laser-based displays.

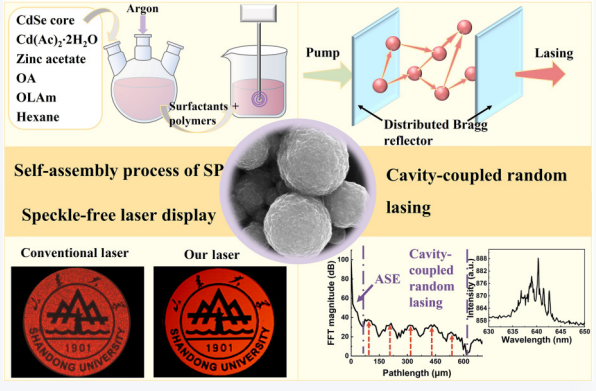

KEYWORDS: CdSe, nanoplatelet, self-assembly, cavity coupled random lasing, speckle-free display

1 Introduction

Laser displays are highly sought after for their ability to produce exceptionally bright, vivid, and true-to-life colors [1–3]. Due to the narrow emission linewidth of lasers, they offer a wider color gamut [4–6] than traditional display technologies, allowing for more precise and saturated color reproduction, which leads to sharper images and greater contrast [7, 8]. Additionally, laser displays are more energy-efficient since lasers can generate the required wavelengths directly without relying on filters or backlighting, thus reducing energy losses [9]. When combined with semiconductor nanocrystal-based lasers, which offer tunable emission and high color purity, the result is a display technology capable of delivering superior visual performance, cost-effective manufacturing, and versatile design options [8, 10–13].

Received: September 12, 2024; **Revised:** November 18, 2024
Accepted: December 4, 2024

✉Address correspondence to yuan.gao@sdu.edu.cn

CdSe nanoplatelets (NPLs), a type of two-dimensional semiconductor nanocrystals, also known as colloidal quantum wells, provide several distinct advantages as optical gain media for lasing applications over conventional zero-dimensional colloidal quantum dots [14–16]. One key advantage is their narrow photoluminescence (PL) emission linewidth, arising from their uniform thickness, which leads to reduced inhomogeneous broadening and high spectral purity. Additionally, CdSe NPLs exhibit reduced Auger recombination, minimizing non-radiative losses and improving optical gain performance [13, 17, 18]. Combined with their increased gain cross section [19], CdSe NPLs are highly efficient for lasing, offering lower thresholds and enhanced output efficiency [20–22].

However, the high spatial coherence of lasers can lead to significant speckle formation, compromising display quality. Random lasers (RLs), which rely on multiple scattering feedback in disordered media, have been shown to achieve speckle-free imaging [23–26]. This multiple scattering creates complex modes but can still result in narrow emission peaks. Due to random scattering feedback, RLs exhibit low spatial coherence while maintaining

narrow spectral linewidths, making them suitable for speckle-free laser displays. Nonetheless, RLs face challenges such as lower brightness and poor directivity, which limit their applicability in display systems.

To address these limitations, we developed a strategy to achieve random lasing in a single medium while coupling the random laser to directional optical cavity modes. This approach maintains the narrow spectral width and low spatial coherence characteristic of RLs while imparting directivity to the emitted light. To achieve this, we synthesized CdSe/CdZnS core/shell NPLs using the hot-injection method and created supraparticles (SPs) through the gradual evaporation of oil-in-water emulsion droplets. The larger size of the SPs, compared to individual nanocrystals, enhances light–matter interactions and scattering among the SPs [27–29]. These SPs act as both scattering centers and gain media to achieve random lasing. To direct the typically omnidirectional random lasing emission, we integrated a Fabry–Pérot (FP) cavity with the SPs, promoting directional output. This allowed us to achieve directional emission without the need for external optical lenses and a speckle-free projection display with improved image uniformity, reducing speckle contrast from 0.5 to 0.05. This research shows strong potential for advancing nanocrystal-based lasers and speckle-free display technologies.

2 Experimental

2.1 Materials

The chemicals used for NPL synthesis and SP formation are listed below: cadmium nitrate tetrahydrate (Macklin, 99%), sodium myristate (Macklin, > 98%), cadmium acetate dihydrate ($Cd(Ac)_2{\cdot}2H_2O$) (Sigma-Aldrich, 99.99%), zinc acetate (99.99%), sodium myristate (Macklin, > 98%), selenium powder (Aldrich, 99.5%), 1-octanethiol (Sigma-Aldrich, ≥ 98.5%), sodium dodecyl sulfate (SDS, Sigma-Aldrich, ≥ 98.5%), dextran from *Leuconostoc mesenteroides* (Sigma-Aldrich, M_r ≈ 200,000), cyclohexane (anhydrous, 99.5%), 1-octadecene (ODE, Macklin, > 90%), oleic acid (Macklin, 90%), ethanol (99.5%), n-hexane (> 99%), methanol (≥ 99.7%), and acetone (> 99%).

All chemicals were used without further purification.

2.2 Preparation

2.2.1 Preparation of Cd-myristate and synthesis of the 4 ML CdSe core NPLs and 4 ML CdSe/CdZnS core/shell NPLs

Details are given in the Electronic Supplementary Material (ESM).

2.2.2 Synthesis of the SPs

The synthesis was carried out in the open air according to procedures in Refs. [30, 31]. 1 mL of cyclohexane was added to 7 mg of CdSe/CdZnS core/shell NPLs. Then, a water solution was prepared with 10 mL of milli-Q water containing 60 mg of SDS, 0.4 g of dextran, and the CdSe/CdZnS core/shell NPLs. Emulsification was performed at 7500 rpm using a homogenizer with a rotor-stator device. The emulsion was then collected in a cylindrical beater and stirred at 68 °C for 4 h, and the top was covered with a secondary film penetrated by 1 mm holes to allow all cyclohexane to evaporate. By spherical confinement of evaporating droplets, NPLs were pushed together to form SPs. Following evaporation, the SPs were precipitated by centrifugation (3000 rpm, 20 min) to discard the supernatant containing excess surfactant and glucan. The SPs were then dispersed in Milli-Q water. To test the samples, the SP solution was dropped on the silicon substrate, and then the water phase was evaporated to deposit the SPs on the substrate.

2.3 Optical characterization

A 532 nm nanosecond pulsed laser was focused onto FP cavity by an objective (TU Plan EWLD 50×, Nikon). At above threshold, the resulting random lasing passed through the same objective and reached a digital micromirror device (DMD). After DMD modulation, it then went through a 4-f system (comprised of a 175 mm focal length lens and a 200 mm focal length lens), followed by a 550 nm long-pass filter before reaching the white screen, as depicted in Fig. 4(a).

3 Results and discussion

3.1 Assembly of core/shell nanoplatelets into SPs

Firstly, we modified the synthesis method, based on previous research [32], to produce CdSe/CdZnS core/shell NPLs using the hot-injection method with all-solution processing. Transmission electron microscopy (TEM) imaging of NPLs is depicted in Fig. 1(a). The full width at half maximum (FWHM) of the PL from core/shell NPLs is approximately 28.67 nm, notably wider than the FWHM (12.95 nm) of core NPLs. Importantly, the absorption spectrum of core/shell NPLs exhibits two distinct peaks: the heavy-hole (HH) peak at 615 nm and the light-hole (LH) peak at 562 nm. This spectrum demonstrates a clear red shift in each transition peak following the formation of the core/shell structure, indicating a reduction in the quantum confinement effect due to an increase in thickness.

The colloidal stability of NPLs in nonpolar solvents, provided by oleic acid ligands on their surface, is crucial for balancing spatial repulsion and van der Waals attraction to establish initial equilibrium assembly. These NPL dispersions self-assemble by evaporating the nonpolar phase of an oil-in-water emulsion, yielding near-spherical SPs (see Section 2 for details). A schematic diagram of the SP synthesis process is depicted in Fig. 1(c). Diluted NPL dispersions are added to a water solution containing a surfactant, which acts as a spatial stabilizer but can also render the solution viscoelastic. Using a homogenizer with a rotor-stator device, we emulsify the two-phase system formed by water and oil solutions, resulting in dispersed liquid droplets of NPLs floating in water. After 4–6 h at 68 °C, cyclohexane evaporates, limiting the NPLs to a smaller volume and forming solid SPs (Fig. 1(d)). By controlling the homogenizer's stirring rate and the initial volume fraction of NPLs in the oil phase, the sizes of SPs can be adjusted between 100 and 500 nm (Fig. 1(d) and Fig. S1(a) in the ESM), exhibiting a spherical morphology. The PL and absorption spectra of the corresponding SPs are consistent with those of CdSe/CdZnS NPLs, indicating that the assembled CdSe/CdZnS NPL-SPs remain unchanged. To gain further insight into the self-assembled superstructure, we conducted high-angle annular dark-field scanning transmission electron microscopy (HAADF-STEM) scanning on a single 300 nm diameter SP (Fig. 1(f)). The NPLs inside the CdSe/CdZnS NPL-SPs interdigitated with neighbouring NPLs, exhibiting a less ordered arrangement compared to those outside the SPs. The NPLs slightly rotated in-plane (orthogonal to the column direction) with respect to their adjacent NPLs in the same columns. This bending effect was most noticeable for the

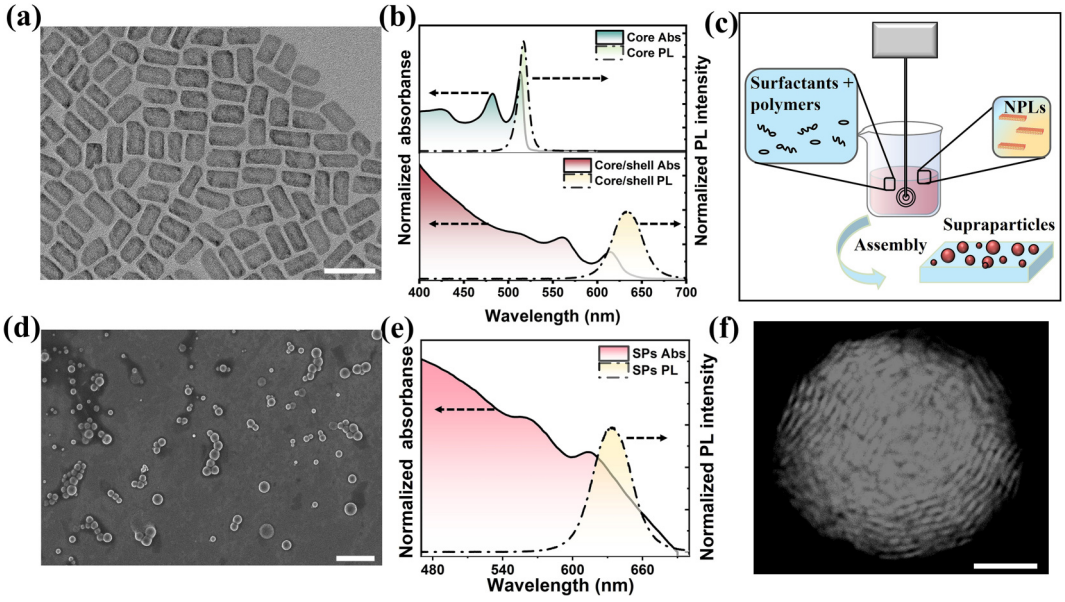

Figure 1 Formation of SPs. (a) The high-resolution TEM image of the core/shell NPLs. Scale bar: 50 nm. (b) Absorption and PL spectra comparison between core and core/shell NPLs. (c) Schematic diagram of SPs self-assembly process via oil-in-water emulsion. (d) The SEM image of the SPs. Scale bar: 2 μm. (e) Absorption and PL spectra of the SPs. (f) The HAADF-STEM image revealing a single SP. Scale bar: 100 nm.

columns that are closer to the confinement boundary, which was most likely induced by the spherical boundary effect of the slowly drying emulsion droplets [33].

3.2 RLs from CdSe/CdZnS NPL-SP films

To analyze the optical gain behavior of CdSe/CdZnS NPL-SPs, we pumped a CdSe/CdZnS NPL-SP film on a quartz substrate using a nanosecond (ns) pulsed laser beam (532 nm, 20 Hz). The film was optically pumped in a quasi-continuous state, as the pulse duration is comparable to the gain lifetime of the NPLs [34]. When the excitation intensity is sufficiently high, population inversion occurs, leading to amplified spontaneous emission (ASE) within the CdSe/CdZnS NPL-SPs, as shown in Fig. S2(a) in the ESM. At low pump fluence (< 291 μJ·cm^{-2}), the film emits typical PL with a single-peak spectrum centered around 627 nm. When the pump fluence exceeds 291 μJ·cm^{-2}, an ASE emission peak appears at 637 nm, with a significantly reduced linewidth of 5.5 nm, showing a 10 nm red shift relative to the PL maximum (Fig. S2(b) in the ESM). Since the CdSe/CdZnS NPL-SP film, prepared via solution methods, lacks a predefined laser cavity, the lasing effect likely originates from random scattering caused by grain boundaries or other scattering centers within the film. As the pump power is further increased, narrow peaks with FWHM below 1 nm appear in the emission spectrum, as shown in Fig. 2(b). The inset of Fig. 2(b) plots the relationship between normalized intensity and pump fluences, where the curve exhibits a kink at the threshold P_{th} = 357 μJ·cm^{-2}, signifying a transition from spontaneous emission to lasing.

In random lasing, Mie scattering is dominant and favorable due to its strong and efficient scattering properties [35]. The scattering behavior depends on the particle size parameter $x = 2\pi r/\lambda$ [36] (r is the particle radius and λ is the wavelength of light). In our system, the SPs have a size distribution ranging from 150 to 550 nm, with a central size of approximate 300 nm, as shown in Fig. S1(b) in the ESM. This range is particularly well-suited for random lasing at a wavelength of 630 nm, as it corresponds to $x \sim 1$, placing the system in the resonance regime. This maximizes scattering efficiency while maintaining sufficient randomization of scattering paths for robust feedback [37].

To analyze the optical feedback of RLs, we applied fast Fourier transform (FFT) to the emission spectrum above the threshold of CdSe/CdZnS NPL-SP films, as shown in Fig. 2(c). The emission of the complex lasing combines multiple simultaneous processes, including ASE generation and coherent random lasing [20, 38]. In the FFT analysis, at a path length of 60 μm, the beam experiences reduced scattering in the gain medium, resulting in ASE with incoherent stimulated emission. As the beam undergoes further scattering, coherent optical feedback is established, leading to the observation of random lasing between 60 and 600 μm.

SPs serve as both scattering and optical gain media within the CdSe/CdZnS NPL-SP films. Light undergoes multiple scattering events within the SPs film, forming closed loops (Fig. 2(a)). These closed loops resemble a ring resonator, providing coherent feedback that enables laser amplification and resonance. This occurs because the path length and dwell time of light within the gain medium are extended due to the multiple scattering, effectively amplifying the optical field and facilitating the formation of random lasing. Due to these "random walks", various closed loops form, corresponding to the randomly distributed peaks in the FFT spectra (Fig. 2(c)), achieving optical gain and resulting in random lasing. Additionally, the emission spectra vary significantly at different pumping locations (Fig. S3 in the ESM), further confirming the presence of random lasing in CdSe/CdZnS NPL-SP films.

3.3 Coupling the RLs with FP cavities

As shown in Fig. S4 in the ESM, the laser spot generated from the RLs of the CdSe/CdZnS NPL-SP film disperses widely on the screen, necessitating the use of an optical lens for collection and collimation. Therefore, developing RLs with directional emission and reducing reliance on collimating optics become crucial. To address this challenge, we integrate the SPs into an FP cavity to promote the longitudinal optical feedback, resulting in directional light emission. As depicted in Fig. 2(d), the RL-FP (random laser coupled with Fabry–Pérot cavity) laser consists of CdSe/CdZnS NPL-SP film sandwiched between two distributed Bragg reflectors (DBRs), supporting transverse RL and longitudinal FP resonance.

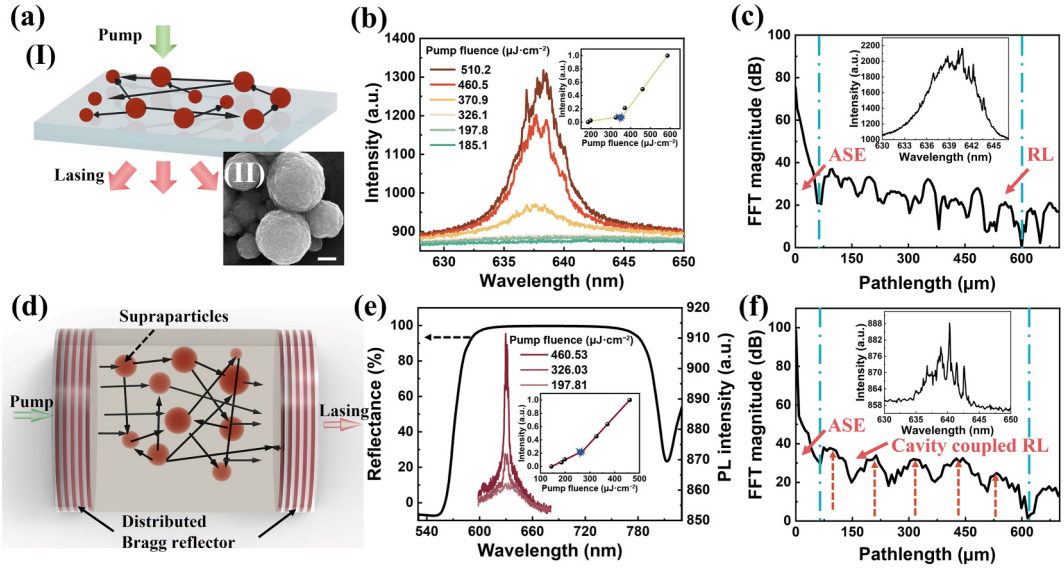

Figure 2 Characterization of lasing from CdSe/CdZnS NPL-SP film and the RL-FP architecture. (a) (I): Schematic representation of the RL formation principle. (II): SEM image of the SPs with a scale bar of 200 nm. (b) Evolution of the emission spectra as a function of pump fluence. The inset shows the emission intensities with increasing pump fluence. (c) FFT analysis of the RL spectrum above the threshold. The corresponding lasing spectrum is shown in the inset. (d) Schematic illustration of the RL-FP laser configuration. (e) Reflection spectrum of the DBR (black line) alongside the emission spectra at increasing pump fluences. The inset shows the emission intensities as a function of pump fluence. (f) FFT analysis of the emission spectrum above the threshold of the RL-FP laser configuration. The corresponding lasing spectrum is shown in the inset.

The former is controlled by the gain medium and scattering, while the latter is determined by the stop band of DBRs. The stop band of DBRs ranges from 600 to 800 nm with a reflectivity greater than 99.9%. The emission spectra of CdSe/CdZnS NPL-SPs fall entirely within the high reflection region of the DBRs (Fig. 2(e)), facilitating effective coupling between the CdSe/CdZnS NPL-SPs and the FP cavities.

The lasing characteristics of our RL-FP lasers were investigated under optical excitation. At low pump fluences, there is only a broad emission peak dominated by spontaneous emission (Fig. S5 in the ESM). As the pumping fluence increases to 273 μJ·cm^{-2}, a series of discrete sharp peaks emerge in the range of 625–635 nm, with an FWHM of approximate 1 nm. The inset of Fig. 2(e) illustrates the normalized emission intensity as a function of pump fluences, showing a clear transition from spontaneous emission to stimulated emission, indicating the onset of lasing action. A laser spot with a diameter of less than 5 mm is observed on a screen positioned 15 cm away from the CdSe/CdZnS NPL-SP RL-FP laser, demonstrating the highly directional nature of emission (see the inset of Fig. S4 in the ESM). This directionality arises because the random lasing modes that align with the FP cavity oscillation are enhanced, resulting in highly directional lasing perpendicular to the cavity surface.

To gain insight into the lasing mechanism of the RL-FP laser, we performed an FFT analysis on the lasing spectrum above the threshold, as shown in Fig. 2(f). After coupling the RL from SPs with the FP cavity, the random lasing modes that match the FP cavity oscillation are promoted, resulting in equally spaced envelopes, corresponding to the longitudinal modes of the FP cavity, which enclose the random lasing modes (see the inset of Fig. 2(f)). This behavior is distinct from the FFT of the RL from the NPL-SP film, which shows only randomly distributed modes (see the inset of Fig. 2(c)). Therefore, in our RL-FP laser, random lasing modes are coupled with and selected by the FP cavity, enhancing the directionality of the lasing output.

To investigate the effect of pumping locations on CdSe/CdZnS RL-FP lasers, we tested the emission spectra at three different pumping locations. The peak position and mode distribution vary significantly with each location, as shown in Figs. 3(a)–3(f). This variation showcases the random nature of the emission, which is critical for preserving low spatial coherence.

3.4 Speckle-free display using CdSe/CdZnS NPL-SP RL-FP lasers

Laser is favored for display purposes due to its narrow emission line width and remarkable brightness. However, the high spatial coherence of lasers often leads to undesirable speckles, reducing display quality. Fortunately, RLs with low spatial coherence offer a solution, producing speckle-free images suitable for displays. To demonstrate this, we compared the illumination of a He:Ne laser, known for its high spatial coherence, with our CdSe/CdZnS NPL-SP RL-FP laser. Figures 4(c) and 4(d) depict the results of illuminating the 1951 U.S. Air Force (USAF) resolution test pattern with the He:Ne laser and the RL-FP laser, respectively. While the image illuminated by the He:Ne laser exhibits uneven intensity distribution and noticeable speckles, the RL-FP laser produces clear and uniform speckle-free imaging.

To visually demonstrate the capability of improving image quality and achieving a speckle-free display using the RL-FP lasers, we constructed a laser projector employing a DMD. Figure 4(a) illustrates the typical configuration for the laser projection display. We employed a 50× objective lens to collect the light emission from our laser device. However, limited by the numerical aperture of the objective, this setup allows for partial light collection, resulting in operational complexity and significant laser energy wastage (see Fig. 4(a)(II)). In contrast, the highly directional laser beam generated by CdSe/CdZnS NPL-SP RL-FP lasers can directly illuminate the pattern. The corresponding pattern is then projected onto the white screen through the 4-f system (see Fig. 4(a)(I)). As depicted in Fig. 4(e), speckles are observed in the projection images under He:Ne

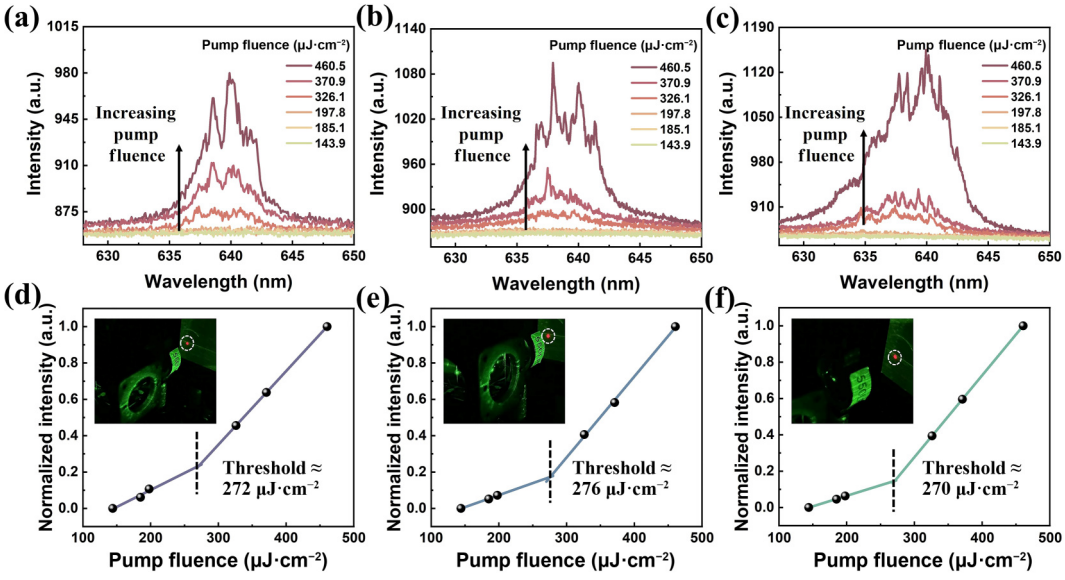

Figure 3 Output at various positions of the CdSe/CdZnS NPL-SP RL-FP laser. (a)–(c) The evolution of emission spectra with pump fluences. (d)–(f) The relationship between normalized intensities and pump fluences. The insets showcase the snapshots of the corresponding lasing spots (dashed circles).

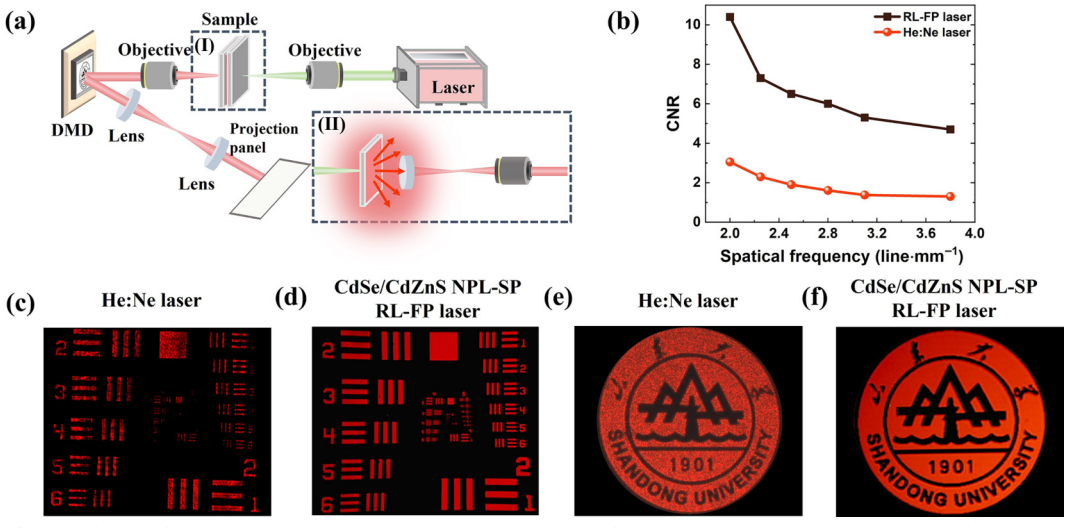

Figure 4 Speckle-free laser display achieved with the CdSe/CdZnS NPL-SP RL-FP laser. (a) Schematic diagram illustrating the experimental setup utilizing RL-FP laser as lighting sources. (b) CNR versus spatial frequency of the features on the AF resolution test chart for the He:Ne laser and CdSe/CdZnS NPL-SP RL-FP laser. Images of a 1951 USAF resolution test card captured under the illumination of (c) a He:Ne laser and (d) CdSe/CdZnS NPL-SP RL-FP laser. Projected images using (e) He:Ne laser and (f) CdSe/CdZnS NPL-SP RL-FP laser.

laser illumination. Conversely, under the illumination of CdSe/CdZnS NPL-SP RL-FP lasers, a clear image with uniform intensity is observed on the screen (Fig. 4(f)). These results indicate that our RL-FP lasers can generate directional low-coherence lasing, enhancing image quality and achieving speckle-free displays.

To quantitatively compare the speckle suppression capabilities of the laser sources, we calculate the speckle contrast $C = \sigma/\langle I \rangle$ [23], where σ represents the standard deviation of the intensity and $\langle I \rangle$ is the average intensity from the image. The decrease in speckle contrast indicates a reduction in spatial coherence and an increase in the signal-to-noise ratio. For the He:Ne laser, speckle contrasts are C = 0.4943 and 0.5143 (Figs. 4(c) and 4(e)). When switching to our RL-FP lasers, speckle contrasts decrease by an order of magnitude to C = 0.0441 and 0.0473 (Figs. 4(d) and 4(f)). In addition, we demonstrate that the ability of a random laser to prevent speckle formation translates to improved image quality by the 1951 USAF resolution test pattern. Image quality can be quantitatively compared using the contrast-to-noise ratio (CNR), which is defined as $(\langle I_f \rangle - \langle I_b \rangle)/((\sigma_f + \sigma_b)/2)$, where $\langle I_f \rangle$ is the average intensity of the feature of interest, $\langle I_b \rangle$ is the average intensity of the surrounding background, and σ is the standard deviation of the pixel intensity. CNR describes the identifiability of features of interest in a given context. As shown in Fig. 4(b), CNR decreases with the increase of spatial frequency, and the CNR of the laser we prepared is always higher than that of the He:Ne laser. In short, images illuminated by CdSe/CdZnS NPL-SP RL-FP lasers have the lowest speckle contrast and highest CNR, which indicates a good imaging performance. This substantial improvement is primarily due to the efficient outcoupling of random lasing modes, which reduces spatial coherence and thus suppresses speckle.

4 Conclusions

In conclusion, our study demonstrates that integrating

CdSe/CdZnS core/shell NPL-SPs with an FP cavity enables directional low-coherence emission, achieving a threshold of 270 μJ·cm^{-2} under quasi-continuum optical pumping. FFT analysis of the RL spectrum reveals that after coupling with the FP cavity, equally spaced envelopes containing random optical paths emerge, indicating effective coupling of the RL modes with the FP cavity. By using our RL-FP laser as an illumination source, we successfully achieve speckle-free displays with enhanced image uniformity. Our research holds significant promise for advancing the development of nanocrystal-based lasers and speckle-free laser displays.

Electronic Supplementary Material: Supplementary material (preparation of cadmium myristate ($Cd(myr)_2$), synthesis of 4 ML CdSe core NPLs, synthesis of 4 ML CdSe/CdZnS core/shell NPLs, characterizations, SEM image of SPs emulsified by homogenizer, emission spectra above the threshold at different locations of the CdSe/CdZnS NPL-SP film, schematic illustration of a laser spot generated from the random laser of the CdSe/CdZnS NPL-SP film, and schematic illustration of a lasing spot generated from the random laser of the CdSe/CdZnS NPL-SP laser above the threshold) is available in the online version of this article at https://doi.org/10.26599/NR.2025.94907170.

Data availability

All data needed to support the conclusions in the paper are presented in the manuscript andr the Electronic Supplementary Material. Additional data related to this paper may be requested from the corresponding author upon request.

Acknowledgements

This work was financially supported by the National Natural Science Foundation of China (No. 62205180), the Natural Science Foundation of Shandong Province (No. ZR2022QF029), and the Taishan Scholar Program of Shandong Province (Young Scientist).

Declaration of competing interest

All the contributing authors report no conflict of interests in this work.

Author contribution statement

Y. G., B. Q. S., and X. Z.: Initiating the study. C. L. W.: Fabricating and characterizing the samples. C. L. W. and H. X. Z.: Performing the optical characterizations. C. L. W. and Y. G.: Writing the manuscript.

Use of AI statement

None.

References

[1] Li, H. J.; Feng, Y. F.; Zhu, M. Y.; Gao, Y.; Fan, C.; Cui, Q. P.; Cai, Q. T.; Yang, K.; He, H. P.; Dai, X. L. et al. Nanosurface-reconstructed perovskite for highly efficient and stable active-matrix light-emitting diode display. *Nat. Nanotechnol.* **2024**, *19*, 638–645.

[2] Liao, S. X.; Yang, Z. Z.; Lin, J. D.; Wang, S. X.; Zhu, J. W.; Chen, S. X.; Huang, F.; Zheng, Y. H.; Chen, D. Q. A hierarchical structure perovskite quantum dots film for laser-driven projection display. *Adv. Funct. Mater.* **2023**, *33*, 2210558.

[3] Kim, J.; Roh, J.; Park, M.; Lee, C. Recent advances and challenges of colloidal quantum dot light-emitting diodes for display applications. *Adv. Mater.* **2024**, *36*, 2212220.

[4] Liao, H. X.; Zhao, M.; Zhou, Y. Y.; Molokeev, M. S.; Liu, Q. L.; Zhang, Q. Y.; Xia, Z. G. Polyhedron transformation toward stable narrow-band green phosphors for wide-color-gamut liquid crystal display. *Adv. Funct. Mater.* **2019**, *29*, 1901988.

[5] Liu, X.; Huang, Z.; Zang, J. F. All-dielectric silicon nanoring metasurface for full-color printing. *Nano Lett.* **2020**, *20*, 8739–8744.

[6] Miyata, S.; Iso, Y.; Isobe, T. Green photoluminescence of perovskite $CsPb(Br_{1-x}I_x)_3$ nanocrystals for wide color gamut displays. *ACS Omega* **2019**, *4*, 15067–15073.

[7] Qin, Z. S.; Gao, C.; Gao, H. K.; Wang, T. Y.; Dong, H. L.; Hu, W. P. Molecular doped, color-tunable, high-mobility, emissive, organic semiconductors for light-emitting transistors. *Sci. Adv.* **2022**, *8*, eabp8775.

[8] De, J. B.; Zhao, R. Y.; Yin, F.; Gu, C. L.; Long, T.; Huang, H.; Cao, X.; An, C. B.; Liao, B.; Fu, H. B. et al. Organic polaritonic light-emitting diodes with high luminance and color purity toward laser displays. *Light Sci. Appl.* **2024**, *13*, 191.

[9] Yin, K.; Hsiang, E. L.; Zou, J. Y.; Li, Y. N. Q.; Yang, Z. Y.; Yang, Q.; Lai, P. C.; Lin, C. L.; Wu, S. T. Advanced liquid crystal devices for augmented reality and virtual reality displays: Principles and applications. *Light Sci. Appl.* **2022**, *11*, 161.

[10] Cifci, O. S.; Yoder, M. A.; Xu, L.; Chen, H.; Beck, C. J.; He, J. W.; Koscher, B. A.; Nett, Z.; Swabeck, J. K.; Paul Alivisatos, A. et al. Luminescent concentrator design for displays with high ambient contrast and efficiency. *Nat. Photonics* **2023**, *17*, 872–877.

[11] Azizov, R.; Sinev, I.; Işık, F.; Shabani, F.; Pushkarev, A.; Yurdakul, I.; Delikanli, S.; Demir, H. V.; Makarov, S. Direct laser writing of resonant periodic nanostructures in thin light-emitting films of CdSe/CdZnS core/shell nanoplatelets. *Appl. Phys. Lett.* **2022**, *121*, 223301.

[12] Chun, F. J.; Zhang, B. B.; Gao, Y. Y.; Wei, X. H.; Zhang, Q.; Zheng, W. L.; Zhou, J. K.; Guo, Y.; Zhang, X.; Xing, Z. F. et al. Multicolour stretchable perovskite electroluminescent devices for user-interactive displays. *Nat. Photonics* **2024**, *18*, 856–863.

[13] Dabard, C.; Guilloux, V.; Gréboval, C.; Po, H.; Makke, L.; Fu, N. Y.; Xu, X. Z.; Silly, M. G.; Patriarche, G.; Lhuillier, E. et al. Double-crowned 2D semiconductor nanoplatelets with bicolor power-tunable emission. *Nat. Commun.* **2022**, *13*, 5094.

[14] Diroll, B. T.; Guzelturk, B.; Po, H.; Dabard, C.; Fu, N. Y.; Makke, L.; Lhuillier, E.; Ithurria, S. 2D II-VI semiconductor nanoplatelets: From material synthesis to optoelectronic integration. *Chem. Rev.* **2023**, *123*, 3543–3624.

[15] Zhang, L. X.; Pan, X. Y.; Liu, L.; Ding, L. M. Star perovskite materials. *J. Semicond.* **2022**, *43*, 030203.

[16] Grim, J. Q.; Christodoulou, S.; Di Stasio, F.; Krahne, R.; Cingolani, R.; Manna, L.; Moreels, I. Continuous-wave biexciton lasing at room temperature using solution-processed quantum wells. *Nat. Nanotechnol.* **2014**, *9*, 891–895.

[17] Rowland, C. E.; Fedin, I.; Zhang, H.; Gray, S. K.; Govorov, A. O.; Talapin, D. V.; Schaller, R. D. Picosecond energy transfer and multiexciton transfer outpaces auger recombination in binary CdSe nanoplatelet solids. *Nat. Mater.* **2015**, *14*, 484–489.

[18] Brumberg, A.; Watkins, N. E.; Diroll, B. T.; Schaller, R. D. Acceleration of biexciton radiative recombination at low temperature in CdSe nanoplatelets. *Nano Lett.* **2022**, *22*, 6997–7004.

[19] Diroll, B. T.; Cassidy, J. P.; Harankahage, D.; Hua, M. C.; Lin, X. M.; Zamkov, M. Large two-photon cross sections and low-threshold multiphoton lasing of CdS/CdSe/CdS quantum shells. *Nanoscale* **2023**, *15*, 18415–18422.

[20] Gao, Y.; Li, M. J.; Delikanli, S.; Zheng, H. Y.; Liu, B. Q.; Dang, C.; Sum, T. C.; Demir, H. V. Low-threshold lasing from colloidal CdSe/CdSeTe core/alloyed-crown type-II heteronanoplatelets. *Nanoscale* **2018**, *10*, 9466–9475.

[21] Li, Q. Y.; Liu, Q. L.; Schaller, R. D.; Lian, T. Q. Reducing the optical gain threshold in two-dimensional CdSe nanoplatelets by the giant oscillator strength transition effect. *J. Phys. Chem. Lett.* **2019**, *10*, 1624–1632.
[22] Li, Q. Y.; Lian, T. Q. A model for optical gain in colloidal nanoplatelets. *Chem. Sci.* **2018**, *9*, 728–734.
[23] Liu, Y. L.; Yang, W. H.; Xiao, S. M.; Zhang, N.; Fan, Y. B.; Qu, G. Y.; Song, Q. H. Surface-emitting perovskite random lasers for speckle-free imaging. *ACS Nano* **2019**, *13*, 10653–10661.
[24] Gao, W.; Wang, T.; Xu, J. T.; Zeng, P.; Zhang, W. F.; Yao, Y. D.; Chen, C. S.; Li, M. J.; Yu, S. F. Robust and flexible random lasers using perovskite quantum dots coated nickel foam for speckle-free laser imaging. *Small* **2021**, *17*, 2103065.
[25] Ma, R.; Rao, Y. J.; Zhang, W. L.; Hu, B. Multimode random fiber laser for speckle-free imaging. *IEEE J. Sel. Top. Quantum Electron.* **2019**, *25*, 0900106.
[26] Redding, B.; Choma, M. A.; Cao, H. Speckle-free laser imaging using random laser illumination. *Nat. Photonics* **2012**, *6*, 355–359.
[27] Chen, W. G.; Wang, L.; Liu, R. X.; Shen, H. B.; Du, J. F.; Fan, F. J. Self-assembled and wavelength-tunable quantum dot whispering-gallery-mode lasers for backlight displays. *Nano Lett.* **2023**, *23*, 437–443.
[28] Marino, E.; Kodger, T. E.; Wegdam, G. H.; Schall, P. Revealing driving forces in quantum dot supercrystal assembly. *Adv. Mater.* **2018**, *30*, 1803433.
[29] Vanmaekelbergh, D.; van Vugt, L. K.; Bakker, H. E.; Rabouw, F. T.; de Nijs, B.; Van Dijk-Moes, R. J. A.; van Huis, M. A.; Baesjou, P. J.; van Blaaderen, A. Shape-dependent multiexciton emission and whispering gallery modes in supraparticles of CdSe/multishell quantum dots. *ACS Nano* **2015**, *9*, 3942–3950.
[30] Montanarella, F.; Urbonas, D.; Chadwick, L.; Moerman, P. G.; Baesjou, P. J.; Mahrt, R. F.; van Blaaderen, A.; Stöferle, T.; Vanmaekelbergh, D. Lasing supraparticles self-assembled from nanocrystals. *ACS Nano* **2018**, *12*, 12788–12794.
[31] Montanarella, F.; Altantzis, T.; Zanaga, D.; Rabouw, F. T.; Bals, S.; Baesjou, P.; Vanmaekelbergh, D.; van Blaaderen, A. Composite supraparticles with tunable light emission. *ACS Nano* **2017**, *11*, 9136–9142.
[32] Altintas, Y.; Gungor, K.; Gao, Y.; Sak, M.; Quliyeva, U.; Bappi, G.; Mutlugun, E.; Sargent, E. H.; Demir, H. V. Giant alloyed hot injection shells enable ultralow optical gain threshold in colloidal quantum wells. *ACS Nano* **2019**, *13*, 10662–10670.
[33] Wang, D.; Hermes, M.; Najmr, S.; Tasios, N.; Grau-Carbonell, A.; Liu, Y.; Bals, S.; Dijkstra, M.; Murray, C. B.; van Blaaderen, A. Structural diversity in three-dimensional self-assembly of nanoplatelets by spherical confinement. *Nat. Commun.* **2022**, *13*, 6001.
[34] Dang, C.; Lee, J.; Breen, C.; Steckel, J. S.; Coe-Sullivan, S.; Nurmikko, A. Red, green and blue lasing enabled by single-exciton gain in colloidal quantum dot films. *Nat. Nanotechnol.* **2012**, *7*, 335–339.
[35] García, P. D.; Ibisate, M.; Sapienza, R.; Wiersma, D. S.; López, C. Mie resonances to tailor random lasers. *Phys. Rev. A* **2009**, *80*, 013833.
[36] Gaio, M.; Peruzzo, M.; Sapienza, R. Tuning random lasing in photonic glasses. *Opt. Lett.* **2015**, *40*, 1611–1614.
[37] Gottardo, S.; Sapienza, R.; García, P. D.; Blanco, A.; Wiersma, D. S.; López, C. Resonance-driven random lasing. *Nat. Photonics* **2008**, *2*, 429–432.
[38] Ryglowski, L.; Cyprych, K.; Mysliwiec, J. The differentiation procedure between amplified spontaneous emission and lasing phenomena. *Opt. Commun.* **2022**, *510*, 127939.